A Fundamental Climate Data Record Derived from AMSR-E, MWRI and AMSR2

Banghai Wu, Yu Wang, Chengzhi Zou, Rui Li, Shi Liu, Guosheng Liu,Yunfei Fu

***Abstract*—Fundamental climate data records (FCDRs) play a vital role in monitoring climate change. This study develops a space-borne passive microwave-based FCDR by recalibrating the Advanced Microwave Scanning Radiometer for Earth Observing System (AMSR-E) on the Aqua satellite, the Microwave Radiometer Imager (MWRI) onboard the Feng-Yun-3B (FY3B) satellite, and the Advanced Microwave Scanning Radiometer-2 (AMSR2) onboard the JAXA's Global Change Observation Mission 1st-Water (GCOM-W1) satellite. Before recalibration, it is found that AMSR-E and AMSR2 observations are stable over time but MWRI drifted colder before May 2015 for most channels. In addition, inter-sensor differences of brightness temperatures are as large as 5 to 10 K. To improve data consistency and continuity, several inter-sensor calibration methods are applied by using AMSR2 as a reference while MWRI bridging AMSR2 and AMSR-E. Double difference method is used to correct calibration biases such as scene temperature-dependent bias, solar-heating induced bias, and systematic constant bias. Hardware differences between sensors are corrected using principal component analysis. After recalibration, the mean biases of both MWRI and AMSR-E are less than 0.4 K compared to the reference and their standard deviations are less than 1 K for all channels. Under oceanic rain-free conditions, the brightness temperature biases are less than 0.2 K for most channels and no significant relative bias drifts were found between sensors for overlapping observations. These statistics suggest that the consistency between these instruments was significantly improved and the derived FCDR could be very useful to obtain long-term water cycle related variables for climate research.**

***Index Terms*—Inter-calibration; AMSR-E, MWRI, AMSR2; FCDR**

I. Introduction

SPACE-BORNE passive microwave (PMW) radiometers have unique advantages in measuring geophysical variables related to global water and energy cycles in the earth-atmosphere system including temperature, water vapor, cloud liquid water, precipitation and surface variables [1]– [7],due to high penetrability with long wavelengths ranging from about 1 mm to 1 m.Until now, PMW measurements have spanned over several decades with multiple sensors onboard different satellites. This makes it possible to develop long-term radiance observations and subsequent retrieval datasets for climate research [8]– [10], or so called fundamental climate data record (FCDR) or climate data records (CDRs). As suggested by US National Research Council committee in 2004 [11], a FCDR or CDR is defined as a time series of measurements of sufficient length, consistency, and continuity. Considering instrumental and orbital differences for different radiometers, an inter-calibration between sensors is vital and should be first carried out in constructing PMW FCDRs.

PMW sensors include imagers and sounders. The first inter-calibration effort for PMW imagers was initiated with the launch of the operational Special Sensor Microwave Imager (SSM/I) instruments during 1987–1997 on DMSP satellites F-8 to F-14 [12]– [14]. These inter-calibration activities, started 30 years ago, continue to be implemented to other radiometers, including the Tropical Rainfall Measuring Mission (TRMM) Microwave Imager (TMI) [15], the Special Sensor Microwave Imager/Sounder (SSMIS) [16], and the most recently the Global Precipitation Measurement (GPM) Microwave Imager (GMI) on GPM satellite [17], and so on. For PMW sounders, inter-calibration at the radiance level started with Microwave Sounding Unit (MSU) in 2006 [5] and Advanced Microwave Sounding Unit (AMSU) in 2011 [7], and the resulting FCDRs have been used for CDR generation for climate change studies [e.g., [7], [8]].

As summarized in [18], inter-calibration approaches can be generally classified into three groups. The first one is the Simultaneous Nadir Overpass (SNO) [19] or Simultaneous Conical Overpass (SCO) approach [20], in which calibration difference is compared for matched pairs of observations from instruments with the same view target and time. The second is statistical analysis [21]– [22], based on the principle that statistical mean observations for different sensors over a period of time and global (or specific) regions are equivalent. The third is double difference method, where the third instrument [23] or a radiometer transfer model [24] is adopted as an intermediate reference. Note that inter-calibration leads to recalibration or inter-calibrated FCDRs when bias correction is applied to the comparing instruments. For example, using SNO pairs, the MSU atmospheric sounding channels onboard TIROS-N through NOAA 14 were successfully recalibrated by Zou et al. [5]– [6]. Using similar method, observations from the Advanced Microwave Sounding Unit-A (AMSU-A) on satellites from NOAA-15 to NOAA-18 and MetOp-A had been consistently inter-calibrated by the same group [7]. Moreover, the GPM constellation radiometers had been well inter-calibrated with the GMI using multiple techniques

Manuscript is submitted on July 3, 2019.(*Corresponding author: Yu Wang.*)
Y. Wang and R. Li are with the School of Earth and Space Sciences, University of Science and Technology of China, Hefei 230026, Anhui, China, and also with CAS Center for Excellence in Comparative Planetology, Hefei 230026, Anhui, China (e-mail: wangyu09@ustc.edu.cn).
B. Wu, S. Liu and Y. Fu are with the School of Earth and Space Sciences, University of Science and Technology of China, Hefei 230026, Anhui, China (e-mail: bh001@mail.ustc.edu.cn).
C. Zou is with the Center for Satellite Applications and Research, NOAA/NESDIS, College Park, MD 20740, USA (e-mail: Cheng-Zhi.Zou@noaa.gov).
G. Liu is with the Department of Earth, Ocean and Atmospheric Science, Florida State University, Tallahassee, FL 32306, USA (e-mail: gliu@fsu.edu).

developed by the GPM Intersatellite Calibration Working Group (X-Cal teams) [25], with the residual biases less than 1K for all sensors/channels after inter-calibration.

As a typical PMW imagery sensor, the Advanced Microwave Scanning Radiometer for Earth Observing System (AMSR-E) has been flown on board the NASA Aqua satellite since its launch in June 2002. It measures brightness temperatures (TBs) at frequencies of 6.925, 10.65, 18.7, 23.8, 36.5 and 89.0 GHz with both vertical and horizontal polarizations [26], which can be used to obtain important terrestrial, oceanic and atmospheric variables [27]– [29]. The AMSR-E ceased operations in October 2011 due to a failure of the rotational antenna spin mechanism. As its successor, the Advanced Microwave Scanning Radiometer-2 (AMSR2) onboard the JAXA's Global Change Observation Mission 1st-Water (GCOM-W1) satellite started operational in May 2012. Comparing to its predecessor, some important improvements have been made in the AMSR2, such as a larger main reflector with 2.0 m diameter for higher resolution, and an additional frequency of 7.3 GHz for terrestrial measurements. Even so, most of the characteristics of the AMSR-E including view angles and other observation channels are still inherited in the AMSR2. As a result, some geophysical retrieval algorithms from the AMSR-E could be directly transferred and applied to the AMSR2. However, the radiance measurements or retrievals from the AMSR-E and AMSR2 are not expected to be easily combined into a FCDR or CDR, because possible differences between them from various aspects, pre-launch or on-orbit calibrations, may lead to discrepancies in observed TBs and subsequent retrievals [30]. More importantly, a temporal-gap about nine months from October 2011 to July 2012 makes it impossible to conduct a direct inter-calibration between the AMSR-E and AMSR2 based on simultaneously overpass matchups. Also, this discontinuity of time series prevents us from constructing the entire FCDR through a simple combination of only AMSR-E and AMSR2 measurements.

Fortunately, this gap can be bridged by measurements from the Microwave Radiometer Imager (MWRI) onboard the Feng-Yun-3B (FY3B) satellite operated continuously since November 2010 by the National Satellite Meteorological Center of China Meteorological Administration (NSMC) [31]. Of particular characteristics, the orbit of the FY3B satellite is close to that of Aqua with a similar inclination angle (98.81° vs 98.14°), close ascending mode (1:40 PM vs 1:30 PM) and orbit altitude (836 km vs 705 km). Furthermore, the frequencies and channels of the MWRI are identical to those of the AMSR-E and AMSR2, though the incident angle is slightly different (53.1° vs. 55°). These same observation channels make it easier to carry out inter-calibration between the MWRI and AMSR-E/AMSR2 without TB correction and regression due to frequency differences [32].

The goal of this study is to inter-calibrate these instruments using the overlapping MWRI as an intermedia reference for developing a PMW TB FCDR. A sequential procedure is used to recalibrate the MWRI and AMSR-E using the AMSR2 as a standard. In this process, MWRI measurements are first adjusted to AMSR2, and then the adjusted MWRI is used to correct the AMSR-E. These bias-corrected or recalibrated TBs finally form a continuous FCDR from the last two decades (from 2002 to 2019) and going forward that could be useful for climate change research.

The rest of the paper is organized as follow. Section II describes data and methodologies. Section III presents results. Finally, Section IV gives conclusions and discussions.

II. Data and Methodology

Both vertically (V) and horizontally (H) polarized channels at five common frequencies from 10.65 GHz to 89.0 GHz on the AMSR-E, AMSR2 and MWRI are inter-calibrated in this study. They are abbreviated as 10V/H, 19V/H, 23 V/H, 37V/H and 89 V/H, respectively. The AMSR2 data used here are the L1R re-sampled swath TB product (version 2) from July 2012 to present derived by JAXA [33], and the AMSR-E data are the L2A re-sampled swath TB product (version 3) provided by the National Snow & Ice Data Center (NSIDC) [34] from July 2002 to October 2011. For the MWRI, the high quality L1 re-sampled swath TB dataset from June 2011 to present provided by NSMC are applied [35].

Prior to inter-calibration, possible system bias for each sensor due to time drift over its lifetime is first checked for later correction, based on vicarious cold reference method developed by Ruf [21]. In this approach, the minimum TB at any channel over the open ocean is related to a fixed sea surface temperature with low water vapor content and could be statistically estimated as an almost invariant parameter with years. Based on this characteristics, it is assumed that any large annual variation of cold point should be simply due to instrument drift over time. Our examination indicate that the AMSR2 and AMSR-E are stable without any significant TB drift over time for most channels except for AMSR2 channels 19V and 89V that have slightly warming trends (not shown). On the other hand, TBs from the MWRI at all channels drifted colder from close to the beginning of the mission until May 2015 (Fig.1), with a 5% significance level by the Mann-Kendall trend test. By a best-fit linear regression, negative trend at each channel is observed. In specific, 10H channel has the smallest drift rate, being -0.14 K/year, while the largest trend is at 89H with -0.7 K/year. For bias drift with these magnificent, TBs at every MWRI channel during this period should be corrected before implementing recalibration procedure as described in the following.

As a first step of inter-calibration between two sensors, SCO matchups are gathered for any two overlapping sensors. To ensure high quality of SCO pairs, the following criteria are applied, similar to Yang et al. [20]. Firstly, all possible SCO pairs should have the same orbital node (i.e. ascending or descending). Secondly, the spatial and time distances should be less than 3 km and 5 min, respectively. Finally, the standard deviation of nine neighboring pixels surrounding a candidate SCO pair must be less than 2K to avoid inhomogeneous background conditions. Using these criteria, 42,766,065 and 50,060,353 SCO pairs between AMSR2 and MWRI during July 2012 to December 2017 are collected for ascending and descending orbits, respectively. For the MWRI and AMSR-E pairs, 10,500,498 and 13,671,552 SCO matchups are found for ascending and descending orbits during the overlapping period from June 2011 to September 2011. Note due to similar scanning geometry and orbits, the SCOs are found distributed nearly globally, offering a full dynamic range for use of instrument inter-calibrations.

Generally, the TB biases between two sensors arise mainly from calibration differences, as well as hardware differences in frequency, earth incident angle (EIA), bandwidth and so on. Since the frequencies are the same for the analyzed instruments, hardware differences mainly reflect EIA and bandwidth differences here. To remove the effect of hardware differences between the AMSR2 and MWRI in their calibration bias correction process, the double difference (DD) method [24] is applied. In this method, simulated TBs are first calculated using a radiative transfer model with the ancillary data corresponding to the observed TBs for the AMSR2 and MWRI, represented respectively by AMSR2$_s$ and MWRI$_s$. Here the used radiative transfer model is a plane-parallel Microwave Radiative Transfer (MWRT) model developed by Liu [36] and then updated in 2006 [37]. The input ancillary data to the model include surface temperatures over land and ocean, wind speed at 10 m height (WS), as well as atmospheric profiles of temperature, relative humidity and cloud liquid water (CLW), taken from the European Centre for Medium-Range Weather Forecasts (ECMWF) Reanalysis Interim (ERA-I). ERA-I provides global atmospheric reanalyses for the period from 1979 to present with the time interval of 6h and spatial resolution of 1° by 1°. Additionally, a surface emissivity atlas TELSEM [38] is used to provide surface emissivity for radiative calculation over land [39]. In this study, DD method are applied over the ERA-I grid resolution. Therefore, SCOs are binned into grid cells with the same 1° by 1° resolution.

To avoid large uncertainty in radiative transfer calculations for those grids having AMSR2-MWRI SCO pairs, several additional quality filters are implemented, as shown in Table I. First, calibration coefficients are derived for clear sky conditions that will have smaller uncertainties. For this purpose, ERA-I CLW should be less than 1 mm and precipitation is eliminated by only allowing observed pixels with TB$_{19V}$ $\leq$ 240K over oceans and TB$_{19V}$-TB$_{37V}$$\leq$10K over land to fall into a grid cells. Secondly, homogeneity requirement is enforced by setting the standard deviation of all the observations in a grid cell to be less than 2 K for vertical polarization channels and 3 K for horizontal polarization channels, respectively. In addition, the WS in ERA-I should be less than 10 m/s for marine grid cells and the observed polarization difference (TB$_V$-TB$_H$) at any frequency should be less than 2 K for terrestrial grid cells.

After simulated TBs are obtained, their differences with observed TBs (MWRI$_o$ and AMSR2$_o$, respectively) are calculated as the residual for each radiometer. The residual difference between sensors, i.e., the double difference DD

$$DD = [(MWRI_o - MWRI_s) - (AMSR2_o - AMSR2_s)] \tag{1}$$

effectively removes the hardware differences between the two sensors and then is used to evaluate the calibration differences for recalibration purposes. Note that the DD results are not critically dependent on the selection of reanalysis input datasets because any errors in the input data are cancelled out in the double difference procedure.

Theoretically, the simulated differences between sensors, (MWRI$_s$-AMSR2$_s$), represent the hardware differences under an ideal condition that the radiative transfer models and input ancillary data perfectly represent the instrument characteristics and atmospheric conditions. However, uncertainties in the radiative model calculations exist. Instead, we use the differences of observations between sensors after the correction of calibration biases (see the next section) to represent hardware differences. Such a representation of hardware difference may also contain errors due to uncertainty of calibration bias correction. To minimize these uncertainties, a Principal Component Analysis (PCA) technique is used to extract main characteristics of hardware difference and properly remove it with additional consideration about possible correlation between various channels [40]. In this procedure, AMSR2 TBs in the AMSR2-MWRI SCO pairs are first decomposed into ten PCs for each channel. It is known that not all PCs are indispensable due to a great deal of redundancy in a set of multi-channel TB observations. In this study, the first five PCs are used which can explain about 99.9% of the total variance. Then by multiple linear regression, each PC is separately estimated by TBs at all MWRI channels and then corresponding regression coefficients are obtained. PCs corresponding to all observations are calculated by applying these coefficients to all the MWRI observations. From these five PCs, finally, TBs equivalent to AMSR2 from MWRI for all channels are reconstructed. It is noteworthy that the PCA method is implemented for ocean and 17 different land cover types, respectively, due to different surface radiative characteristics. Here land type is determined by the IGBP Land Cover Type Classification [41] product, which has been included in MWRI L1 re-sampled swath TB dataset.

III. Results

A. Inter-calibration between the AMSR2 and MWRI

As mentioned above, a DD represents the calibration difference between two sensors. As an example, the spatial distribution of DD at 10V channel for one year (2013) is shown in Fig. 2. Other channels have similar results. Negative DD values from -5 to -10 K are seen over the entire globe, indicating large systematic biases due to calibration differences between the two sensors. Moreover, the biases are found latitudinal-dependent, or so called scene temperature-dependent biases [7]. Of interesting, the biases are distinctly different between ascending and descending swaths, most likely related to differences in solar-heating environment [42]. With these observations, biases and their corrections in DD for any channel are divided into three individual sources: scene temperature-dependent biases, solar-heating induced biases, and systematic constant biases, i.e.,

$$DD = DD_t + DD_s + C \tag{2}$$

here DD_t is the temperature-dependent bias, DD_s is solar heating induced bias, and C is a constant systematic bias.

As suggested by Zou [7], the scene temperature-dependent bias is induced from inaccurate nonlinearity calibration in the calibration equation, and can be eliminated by two-point calibration technique [43]. Fig. 3 shows the variations of DD as a function of MWRI TBs based on cold and warm samples for one year from July 2012 to December 2013. In these plots, the cold and warm samples are confined in the regions near equator (5°S-5°N) and calculated for ascending and descending orbits separately. The samples at cold points are those over the clear sky oceans while the warm samples are collected in terrestrial regions where there are little polarization differences. Such a selection of samples could minimize the effect of other factors such as solar-heating bias on the analysis of scene temperature-dependent bias.

Obvious linear relationship between DD values and TBs are found for almost all channels, except for channel 37H in descending orbits. But this exception has little impact on the following linear correction. Also, the fitting coefficients of the least squares regression line at any channel for ascending orbits are almost identical to that for the descending orbits. This gives us confidence that such temperature-dependent bias can be removed by a first-order approximation of MWRI TB:

$$DD_t = aTB_{MWRI} \tag{3}$$

Here a is an averaged fitting coefficient for ascending and descending modes.

Fig. 3 also shows that the DD differences between ascending and descending orbits are about 1.5K for all channels. This reveals again the existence of the solar-heating induced bias. In fact, similar ascending-descending biases have been detected previously for F16 SSMIS that were diagnosed as calibration errors caused by solar intrusions into the warm calibration load and by thermal emission from the main reflector [44]. Such biases would vary depending on whether the instrument is in the sunlight or the shade. In addition, solar-heating-induced time-varying biases have been observed for the TMI [45]–[47], GMI [48] and microwave sounders MSU/AMSU [7]. The ascending-descending difference in the DD between AMSR2 and MWRI is expected to be similar to the solar-heating induced biases found in previous studies. Since AMSR2 has been found independent from time-varying bias [42], this solar-heating bias is most likely caused by the MWRI.

To address this, Fig. 4 shows an example about the dependence of DD minus DD_t, which represent DD_s, on the orbit time for one year at all MWRI vertical polarization channels. Indeed, there is a clear diurnal cycle in DD_s which increased significantly of more than 2 K during darkness as the cooling procession of the instrument and then dropped rapidly after FY-3B satellite was exposed to sun, corresponding to solar heating process on the instrument. It is worth noting that only those samples with limited solar beta angle (β) ranges from 20° to 22° are collected and averaged over the period from entry to leave the earth shadow here, because the change of β, related to the intensity and direction of solar heating on MWRI, would also lead to the variation of DD_s. In fact, the monthly variations of β and DD_s are examined (not shown), and a significant correlation with correlation coefficient of -0.85 between them is found.

Considering the dependence of the solar-heating biases on eclipse time and β, a "bias lookup table" is generated from statistical results for SCO pairs and applied to obtain the corresponding correction item:

$$DD_s = f(T_e, \beta) \tag{4}$$

In this lookup table, T_e is the time FY-3B spent in Eclipse in unit of minute.

Besides scene temperature-dependent and solar-heating biases, an additional constant systematic bias in DD exists due to different calibration offset or other unknown reasons. This bias varies with different channels (Table II).

After all DD_t, DD_s and C are obtained based on (3), (4), and Table II, their summation, defined as the correction term, is extracted from DD and this is expressed as a residual DD′. If DD′ is close to 0 K, it is considered that the calibration difference between the AMSR2 and MWRI has been mostly eliminated. Fig. 5 gives the variations of DD and DD′ with latitudes at 37V channel as an example. Before correction, for ascending orbits are generally more than -7 K, while those for descending orbits are about -5 K in the Southern Hemisphere and increase poleward to -8 K in the Northern Hemisphere. After correction, DD′ is less than 0.2 K regardless of latitudes and ascending or descending orbits. These results are robust and they are similar for the other channels (not shown). This indicates that our correction method about the calibration difference between two sensors performs well.

As a final step in this inter-calibration process, the PCA technique is applied to remove the difference of the hardware characteristics between the MWRI and AMSR2. The SCO pairs from January 2013 to December 2017 are chosen as the training dataset to obtain the PCA coefficient matrix used to convert MWRI TBs to AMSR2 equivalent TBs, while the others from July 2012 to December 2012 are used as validation dataset. Note that the MWRI TBs after the calibration bias correction are used here. Fig. 6 gives the global distribution of the biases between the final AMSR2-equivalent TB from MWRI and AMSR2 TB in the validation dataset. Over ocean, biases are mostly less than 1 K for all channels, except for the polar zones that have a larger uncertainty possibly due to the disturbance of partly unremoved sea ice to microwave measurements. The statistics results (Table III) further display consistency between the two sensors with a mean bias less than 0.4 K and standard deviation (STD) less than 1 K for all channels. Over the land region, similar consistency is found with a mean bias less than 0.3 K and STD less than 1 K for almost all channels, except for the 10H channel that has somewhat a larger STD of 1.4 K. This 10H channel is known to be sensitive to land surface conditions, so the larger biases, being nearly 1 K, are expected over some terrestrial regions such as Southern Africa and Eastern Europe. Even so, there still are more than 63% areas over land having less than 1 K bias, which results in small mean bias of 0.16 K. Overall, in comparison to the those before correction, the corrected MWRI measurements are much consistent to the AMSR2 TB for all channel with accepted level of inter-satellite biases.

B. Inter-calibration between the AMSR-E and MWRI

Since the corrected MWRI TB can be regarded as AMSR2 equivalent measurement, its differences relative to AMSR-E TB should be caused only by calibration difference without the need to consider hardware differences. This makes the inter-calibration much easier. So, in the SCO pairs between AMSR-E and MWRI, the corrected MWRI TB is used instead of the original MWRI TB. On the other hand, since no distinct solar-heating bias for the AMSR-E was found (not shown), the inaccurate nonlinearity in calibration equation between radiometers, as shown in earlier analyses, is assumed to be the only source contributing to calibration difference. Similar to the scene temperature-dependent bias correction for the MWRI and AMSR2, (5) expressed as:

$$Bias_{AMSRE-MWRI} = b_0 + b_1 TB_{AMSRE} \tag{5}$$

is used to determine the bias correction for the SCO pairs between the corrected MWRI TB and the AMSR-E TB during the period of July 2011 to September 2011. The results for the constant (b_0) and slope (b_1) regression coefficients are shown in Table IV.

To evaluate the performance of the bias correction between the AMSR-E and MWRI, Fig. 7 shows the global distributions of the difference between the corrected AMSR-E and MWRI measurements at all channels for the month of June 2011, and the corresponding statistics are given in Table V. Similar to the inter-calibration results between the AMSR2 and MWRI, the biases between the corrected AMSR-E and MWRI are generally less than 1 K in most areas for most channels, except for the 89GHz channels over the high-latitude oceans and the 23H channel over some terrestrial regions. On average, the mean biases are less than 0.4 K for almost all channels, which are comparable to those between the AMSR2 and MWRI. The standard deviation are under 0.9 K for most channels over ocean and land, though they are larger than 1 K at several low-frequency channels such as the 10H over land. Nevertheless, this is acceptable and similar to those between the AMSR2 and MWRI. Overall, the inter-calibration successfully brings the AMSR-E measurements to be more consistent with MWRI as well as to AMSR2.

C. Performance of the FCDR

Fig. 8 shows the monthly averaged time series of the global ocean means and their anomalies for TBs of the three instruments after recalibration. Note that only those samples over oceanic rain-free conditions were selected in this figure. Such a selection of samples most accurately represents possible residual errors after recalibrations, as possible large discrepancies due to the complexity of microwave signals over the land surface or rainfall conditions are excluded. The monthly mean TBs from different sensors are dominated by similar seasonal cycles, while their anomalies show clearly the performance of the FCDR in terms of inter-sensor biases and anomaly trends after recalibration. Generally, relative shift in the phases of seasonal cycles in the monthly time series could measure discrepancies or jumps between different sensors. However, by using moving t-test, no any significant shift of monthly variation is found at 99% significance level for any two overlapping periods, especially at the three key time points near June 2011 when MWRI starts, October 2011 when AMSR-E stops, and July 2012 when AMSR2 begins. This suggests different sensors connect with each other very well in the monthly mean time series with seasonal cycle. In fact, TB biases between any two sensors are less than 0.2 K at most channels for overlapping months. The exception is for the 89H channel in which biases between AMSR2 and MWRI reach 0.5 K. These small biases can also be clearly seen in the anomaly time series in the same plots. This high consistency indicates that the MWRI as a transfer radiometer has well connected AMSR-E and AMSR2. In other words, the AMSR2-equivalent TBs from MWRI have successfully bridged the gap between those from AMSR-E and AMSR2, allowing a consistent and continuous FCDR from the three sensors.

With the excellent bridge from MWRI, long-term changes in the FCDR can be investigated. In Fig. 8, it is also seen that anomaly trends are generally small for the lower frequency channels, but trends are relatively large for the high frequency channels. This is particularly true after 2012 when large warming trends occurred for high frequency channels. These anomaly trends in FCDR TBs possibly reflect long-term trends in the to-be-retrieved hydrological parameters in the hydrological cycle. This will be a topic in future studies, but the TB trends found here demonstrate the possible impact of the FCDRs on climate change studies.

IV. Conclusions

This study develops a TB FCDR through recalibrating observations from the AMSR-E, MWRI and AMSR2. In this process, the AMSR2 was taken as the reference, and the AMSR-E and MWRI TB were converted to AMSR2-equivalent through inter-sensor bias correction. A critical aspect in this process is that MWRI bridges the gaps between AMSR2 and AMSR-E, allowing a continuous FCDR being developed for climate change studies.

Several inter-calibration methods, including the double difference method, the principal component analysis and the least square estimation, are applied to correct hardware differences between radiometers as well as calibration biases such as scene temperature-dependent bias, solar-heating induced bias, and systematic constant bias, respectively. After recalibration, the biases between them have been significantly reduced. For example, calibration differences between the AMSR2 and MWRI, represented by double difference values, were reduced to less than 0.2 K for most channels from a large value ranging from 5 to 10 K. Moreover, the mean biases and their standard deviations between any two sensors for all channels were less than 0.4 K and 1 K, respectively. The process also reduced a MWRI cold drift over time during June 2011 to May 2015 ranging from -0.14 K/year at 10H channel and -0.70 K/year at 89H channel before recalibration to less than -0.06 K/year after recalibration.

The recalibration results a continuous 16 years of brightness temperature FCDR spanning from June 2002 to December 2018. Mean inter-satellite TB biases between sensors over oceanic rain-free conditions are mostly less than 0.2K. Compared to large inter-satellite differences before recalibration, the FCDR is consistent enough for long-term climate change research.

Though the FCDR performs well over ocean, it is less satisfactory over lands yet, due to the uncertainty and complexity of microwave signals on various land surface conditions. More sophisticated bias correction algorithms are need to improve the TB consistency over land. Nevertheless, the recalibration methods used in this study demonstrate their high abilities in bias corrections. We plan to apply these methods to other radiometers such as the TMI, GMI and SSMI series to enhance the FCDRs by adding long-time and high sampling-rate time series.

Acknowledgment

The views, opinions, and findings contained in this report are those of the authors and should not be construed as an official National Oceanic and Atmospheric Administration or U.S. Government position, policy, or decision.

References

[1] Y. Wang, Y. Fu, G. Liu, Q. Liu, and L. Sun,"A new water vapor algorithm for TRMM Microwave Imager (TMI) measurements based on a log linear relationship,"*Journal of Geophysical Research: Atmospheres*, vol. 114, no. D21, 2009.

[2] Y. Wang, G. Liu, E.-K. Seo, and Y. Fu, "Liquid water in snowing clouds: Implications for satellite remote sensing of snowfall," *Atmospheric research*, vol. 131, pp. 60-72, 2013.

[3] G. Liu and J. A. Curry, "Retrieval of precipitation from satellite microwave measurement using both emission and scattering," *Journal of Geophysical Research: Atmospheres*, vol. 97, no. D9, pp. 9959-9974, 1992.

[4] A. Chang and T. Wilheit, "Remote sensing of atmospheric water vapor, liquid water, and wind speed at the ocean surface by passive microwave techniques from the Nimbus 5 satellite," *Radio Science*, vol. 14, no. 5, pp. 793-802, 1979.

[5] C. Z. Zou et al., "Recalibration of microwave sounding unit for climate studies using simultaneous nadir overpasses," *Journal of Geophysical Research: Atmospheres*, vol. 111, no. D19, 2006.

[6] C.-Z. Zou, M. Gao, and M. D. Goldberg, "Error structure and atmospheric temperature trends in observations from the Microwave Sounding Unit," *Journal of Climate*, vol. 22, no. 7, pp. 1661-1681, 2009.

[7] C. Z. Zou and W. Wang, "Intersatellite calibration of AMSUA observations for weather and climate applications," *Journal of Geophysical Research: Atmospheres*, vol. 116, no. D23, 2011.

[8] S. Po-Chedley, T. J. Thorsen, and Q. Fu, "Removing diurnal cycle contamination in satellite-derived tropospheric temperatures: Understanding tropical tropospheric trend discrepancies," *Journal of Climate*, vol. 28, no. 6, pp. 2274-2290, 2015.

[9] G. S. Elsaesser, C. W. ODell, M. D. Lebsock, R. Bennartz, T. J. Greenwald, and F. J. Wentz, "The multisensor advanced climatology of liquid water path (MAC-LWP)," *Journal of Climate*, vol. 30, no. 24, pp. 10193-10210, 2017.

[10] C.-Z. Zou, M. D. Goldberg, and X. Hao, "New generation of US satellite microwave sounder achieves high radiometric stability performance for reliable climate change detection," *Science advances*, vol. 4, no. 10, p. eaau0049, 2018.

[11] N. R. Council, *Review of NOAA's Plan for the Scientific Data Stewardship Program*. National Academies Press, 2005.

[12] J. P. Hollinger, J. L. Peirce, and G. A. Poe, "SSM/I instrument evaluation," *IEEE Transactions on Geoscience and Remote Sensing*, vol. 28, no. 5, pp. 781-790, 1990.

[13] J. Hollinger, "DMSP special sensor microwave/imager calibration/validation," NAVAL RESEARCH LAB WASHINGTON DC1991.

[14] M. C. Colton and G. A. Poe, "Intersensor calibration of DMSP SSM/I's: F-8 to F-14, 1987-1997," *IEEE Transactions on Geoscience and Remote Sensing*, vol. 37, no. 1, pp. 418-439, 1999.

[15] F. J. Wentz, P. Ashcroft, and C. Gentemann, "Post-launch calibration of the TRMM microwave imager," *IEEE Transactions on Geoscience and Remote Sensing*, vol. 39, no. 2, pp. 415-422, 2001.

[16] B. Yan and F. Weng, "Intercalibration between special sensor microwave imager/sounder and special sensor microwave imager," *IEEE Transactions on Geoscience and Remote Sensing*, vol. 46, no. 4, pp. 984-995, 2008.

[17] R. Chen, H. Erahimi, and W. Linwood, "Three-way inter-satellite radiometric calibration between GMI, TMI and WindSat," in *2016 IEEE International Geoscience and Remote Sensing Symposium (IGARSS)*, 2016, pp. 2036-2039: IEEE.

[18] G. Chander, T. J. Hewison, N. Fox, X. Wu, X. Xiong, and W. J. Blackwell, "Overview of intercalibration of satellite instruments," *IEEE Transactions on Geoscience and Remote Sensing*, vol. 51, no. 3, pp. 1056-1080, 2013.

[19] C. Cao, M. Weinreb, and H. Xu, "Predicting simultaneous nadir overpasses among polar-orbiting meteorological satellites for the intersatellite calibration of radiometers," *Journal of Atmospheric and Oceanic Technology*, vol. 21, no. 4, pp. 537-542, 2004.

[20] S. Yang, F. Weng, B. Yan, N. Sun, and M. Goldberg, "Special Sensor Microwave Imager (SSM/I) intersensor calibration using a simultaneous conical overpass technique," *Journal of Applied Meteorology and Climatology*, vol. 50, no. 1, pp. 77-95, 2011.

[21] C. S. Ruf, "Characterization and correction of a drift in calibration of the TOPEX microwave radiometer," *IEEE Transactions on Geoscience and Remote Sensing*, vol. 40, no. 2, pp. 509-511, 2002.

[22] S. T. Brown and C. S. Ruf, "Determination of an Amazon hot reference target for the on-orbit calibration of microwave radiometers," *Journal of Atmospheric and Oceanic Technology*, vol. 22, no. 9, pp. 1340-1352, 2005.

[23] J. Du et al., "Inter-calibration of satellite passive microwave land observations from AMSR-E and AMSR2 using overlapping FY3B-MWRI sensor measurements," *Remote Sensing*, vol. 6, no. 9, pp. 8594-8616, 2014.

[24] T. Wilheit et al., "Intercalibrating the GPM constellation using the GPM Microwave Imager (GMI)," in *2015 IEEE International Geoscience and Remote Sensing Symposium (IGARSS)*, 2015, pp. 5162-5165: IEEE.

[25] W. Berg et al., "Intercalibration of the GPM microwave radiometer constellation," *Journal of Atmospheric and Oceanic Technology*, vol. 33, no. 12, pp. 2639-2654, 2016.

[26] T. Kawanishi et al., "The Advanced Microwave Scanning Radiometer for the Earth Observing System (AMSR-E), NASDA's contribution to the EOS for global energy and water cycle studies," *IEEE Transactions on Geoscience and Remote Sensing*, vol. 41, no. 2, pp. 184-194, 2003.

[27] E. G. Njoku, T. J. Jackson, V. Lakshmi, T. K. Chan, and S. V. Nghiem, "Soil moisture retrieval from AMSR-E," *IEEE transactions on Geoscience and remote sensing*, vol. 41, no. 2, pp. 215-229, 2003.

[28] G. Spreen, L. Kaleschke, and G. Heygster, "Sea ice remote sensing using AMSRE 89GHz channels," *Journal of Geophysical Research: Oceans*, vol. 113, no. C2, 2008.

[29] M. Kazumori, T. Egawa, and K. Yoshimoto, "A retrieval algorithm of atmospheric water vapor and cloud liquid water for AMSR-E," *European Journal of Remote Sensing*, vol. 45, no. 1, pp. 63-74, 2012.

[30] R. M. Parinussa, T. R. Holmes, N. Wanders, W. A. Dorigo, and R. A. de Jeu, "A preliminary study toward consistent soil moisture from AMSR2," *Journal of Hydrometeorology*, vol. 16, no. 2, pp. 932-947, 2015.

[31] H. Yang, L. Lv, H. Xu, J. He, and S. Wu, "Evaluation of FY3B-MWRI instrument on-orbit calibration accuracy," in *2011 IEEE International Geoscience and Remote Sensing Symposium*, 2011, pp. 2252-2254: IEEE.

[32] L. Hong, W. L. Jones, T. T. Wilheit, and T. Kasparis, "Two approaches for inter-satellite radiometer calibrations between TMI and WindSat," *Journal of the Meteorological Society of Japan*. Ser. II, vol. 87, pp. 223-235, 2009.

[33] T. Maeda, Y. Taniguchi, and K. Imaoka, "GCOM-W1 AMSR2 level 1R product: Dataset of brightness temperature modified using the antenna pattern matching technique," *IEEE Transactions on Geoscience and Remote Sensing*, vol. 54, no. 2, pp. 770-782, 2016.

[34] P. Ashcroft and F. Wentz, "Algorithm theoretical basis document, AMSR level 2A algorithm," *Remote Sensing Systems, Santa Rosa, CA.[Online] RSS Tech. Report*, vol. 121, 2000.

[35] H. Yang et al., "The FengYun-3 microwave radiation imager on-orbit verification," *IEEE Transactions on Geoscience and Remote Sensing*, vol. 49, no. 11, pp. 4552-4560, 2011.

[36] G. Liu, "A fast and accurate model for microwave radiance calculations," *Journal of the Meteorological Society of Japan. Ser. II, vol*. 76, no. 2, pp. 335-343, 1998.

[37] G. Liu, ”Approximation of single scattering properties of ice and snow particles for high microwave frequencies,” *Journal of the atmospheric sciences*, vol. 61, no. 20, pp. 2441-2456, 2004.
[38] F. Aires, C. Prigent, F. Bernardo, C. Jimnez, R. Saunders, and P. Brunel, ”A Tool to Estimate LandSurface Emissivities at Microwave frequencies (TELSEM) for use in numerical weather prediction,” *Quarterly Journal of the Royal Meteorological Society*, vol. 137, no. 656, pp. 690-699, 2011.
[39] A. Okuyama and K. Imaoka, ”Intercalibration of advanced microwave scanning radiometer-2 (AMSR2) brightness temperature,” *IEEE Transactions on Geoscience and Remote Sensing*, vol. 53, no. 8, pp. 4568-4577, 2015.
[40] Y. You, C. Peters-Lidard, J. Turk, S. Ringerud, and S. Yang, ”Improving overland precipitation retrieval with brightness temperature temporal variation,” *Journal of Hydrometeorology*, vol. 18, no. 9, pp. 2355-2383, 2017.
[41] T. R. Loveland and A. Belward, ”The IGBP-DIS global 1km land cover data set, DISCover: first results,” *International Journal of Remote Sensing*, vol. 18, no. 15, pp. 3289-3295, 1997.
[42] H. Lawrence et al., An evaluation of FY-3C MWRI and assessment of the long-term quality of FY-3C MWHS-2 at ECMWF and the Met Office. *European Centre for Medium-Range Weather Forecasts*, 2017.
[43] S. K. Biswas, S. Farrar, K. Gopalan, A. Santos-Garcia, W. L. Jones, and S. Bilanow, ”Intercalibration of microwave radiometer brightness temperatures for the global precipitation measurement mission,” *IEEE Transactions on Geoscience and Remote Sensing*, vol. 51, no. 3, pp. 1465-1477, 2013.
[44] W. Bell et al., ”The assimilation of SSMIS radiances in numerical weather prediction models,” *IEEE Transactions on Geoscience and Remote Sensing*, vol. 46, no. 4, pp. 884-900, 2008.
[45] K. Gopalan, W. L. Jones, S. Biswas, S. Bilanow, T. Wilheit, and T. Kasparis, ”A time-varying radiometric bias correction for the TRMM microwave imager,” *IEEE Transactions on Geoscience and Remote Sensing*, vol. 47, no. 11, pp. 3722-3730, 2009.
[46] S. K. Biswas, K. Gopalan, W. L. Jones, and S. Bilanow, ”Correction of time-varying radiometric errors in TRMM microwave imager calibrated brightness temperature products,” *IEEE Geoscience and Remote Sensing Letters*, vol. 7, no. 4, pp. 851-855, 2010.
[47] A. J. Geer, P. Bauer, and N. Bormann, ”Solar biases in microwave imager observations assimilated at ECMWF,” *IEEE Transactions on Geoscience and Remote Sensing*, vol. 48, no. 6, pp. 2660-2669, 2010.
[48] Q. Xue and L. Guan, ”Identification of Sun Glint Contamination in GMI Measurements Over the Global Ocean,” *IEEE Transactions on Geoscience and Remote Sensing*, 2019.

LIST OF FIGURES

Fig. 1 Time series of monthly cold reference TBs for MWRI at vertical (left panel) and horizontal (right panel) polarization channels from 10GHZ (top) to 89GHZ (bottom). The best-fit regression line from June 2011 to May 2015 and corespoding drift rate for every channel are also written on each panel······9

Fig. 2 The spatial distribution of DD between the MWRI and AMSR2 at 10V channel in 2013 for descending (top panel) and ascending (bottom panel) swaths, respectively······10

Fig. 3 Mean DD with error bar as a function of scene temperature in the period from July 2012 to December 2013 at vertical (left panel) and horizontal (right panel) polarization channels from 10GHZ (top) to 89GHZ (bottom). The regression lines for first-order approximation and fitting coefficients are written on each panel for ascending and descending orbits, respectively······11

Fig. 4 DD_s as a function of orbit time at MWRI vertical polarization channels with solar beta angle ranging from 20° to 22° for one year (2013)······12

Fig. 5 DD and DD′ at 37V channel between MWRI and AMSR2 as a function of latitude for two years from 2013 to 2014······13

Fig. 6 Global distribution of residual biases between AMSR2 TB and corrected MWRI TB for SCO pairs from July 2012 to December 2012 at vertical (left panel) and horizontal (right panel) polarization channels from 10GHZ (top) to 89GHZ (bottom)······14

Fig. 7 Global distribution of residual biases between corrected MWRI TB and AMSR-E TB for SCO pairs in June 2011 at vertical (left pannel) and horizontal(right pannel) polarization channels from 10GHZ (top) to 89GHZ (bottom)······15

Fig.8 The monthly mean inter-calibrated TB time series (lines) with their anomalies (dots) for the three sensors over the 60°S-60°N oceanic rain-free areas at vertical (left panel) and horizontal (right panel) polarization channels from 10GHZ (top) to 89GHZ (bottom)······16

LIST OF TABLES

TABLE I QUALITY FILTERS FOR GRID DATA USED IN DD METHOD······17

TABLE II SYSTEMATIC CONSTANT BIASES BETWEEN THE AMSR2 AND MWRI······17

TABLE III MEAN BIASES AND STANDARD DEVIATION BETWEEN CORRECTED MWRI AND AMSR2 TBS WITHIN THE PERIOD OF JULY 2012 TO DECEMBER 2012 AFTER INTER-CALIBRATION OVER OCEAN AND LAND, RESPECTIVELY······18

TABLE IV REGRESSION COEFFICIENTS FOR DETERMINING BIASES BETWEEN AMSR-E AND CORRECTED MWRI TBS······18

TABLE V MEAN BIASES AND STANDARD DEVIATION BETWEEN CORRECTED MWRI ANDCORRECTED AMSR-E TBS IN JUNE 2011 AFTER INTER-CALIBRATION OVER OCEANS AND LANDS, RESPECTIVELY······19

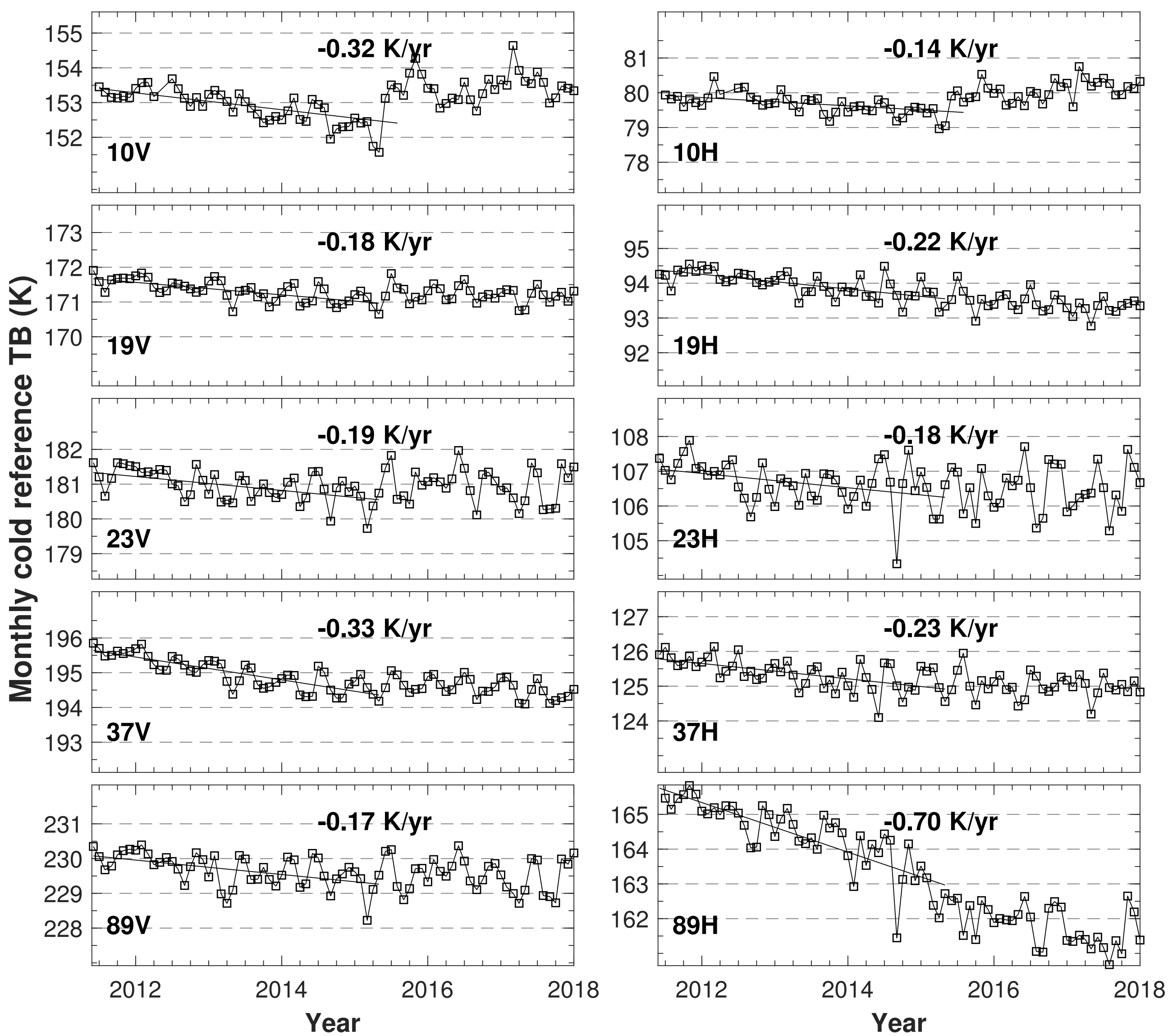

Fig. 1. Time series of monthly cold reference TBs for MWRI at vertical (left panel) and horizontal (right panel) polarization channels from 10GHZ (top) to 89GHZ (bottom). The best-fit regression line from June 2011 to May 2015 and corespoding drift rate for every channel are also written on each panel.

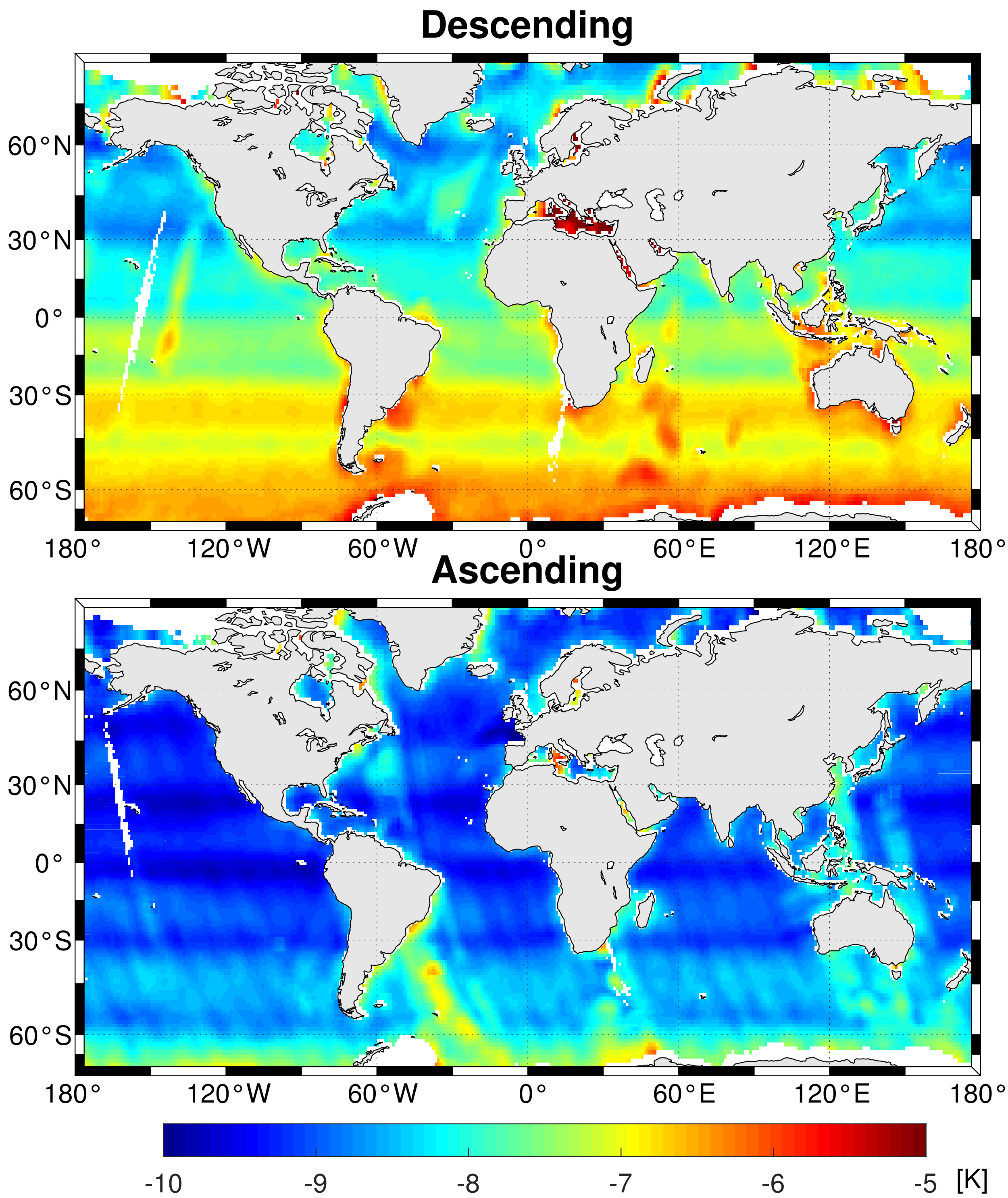

Fig. 2. The spatial distribution of DD between the MWRI and AMSR2 at 10V channel in 2013 for descending (top panel) and ascending (bottom panel) swaths, respectively.

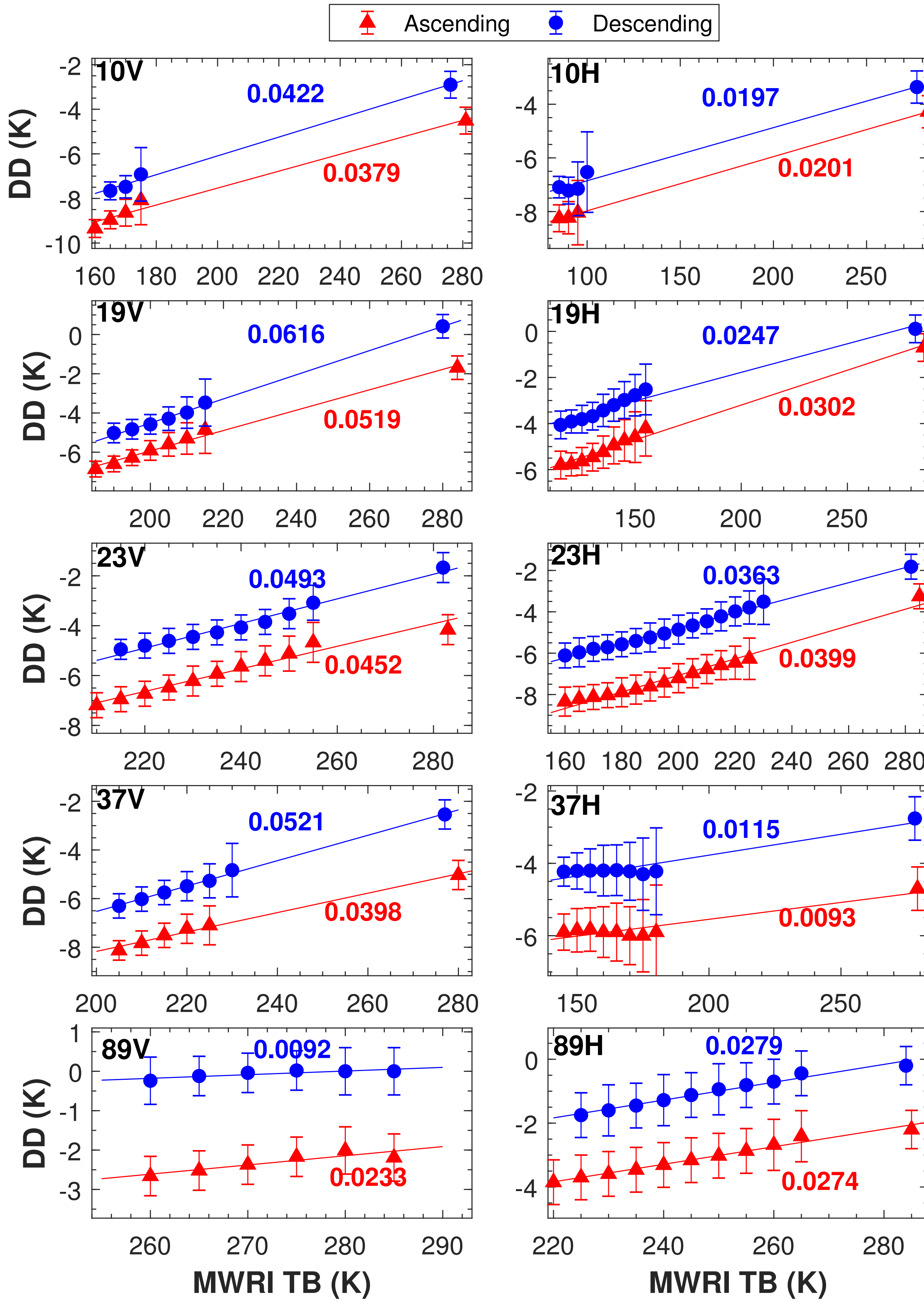

Fig. 3. Mean DD with error bar as a function of scene temperature in the period from July 2012 to December 2013 at vertical (left panel) and horizontal (right panel) polarization channels from 10GHZ (top) to 89GHZ (bottom). The regression lines for first-order approximation and fitting coefficients are written on each panel for ascending and descending orbits, respectively.

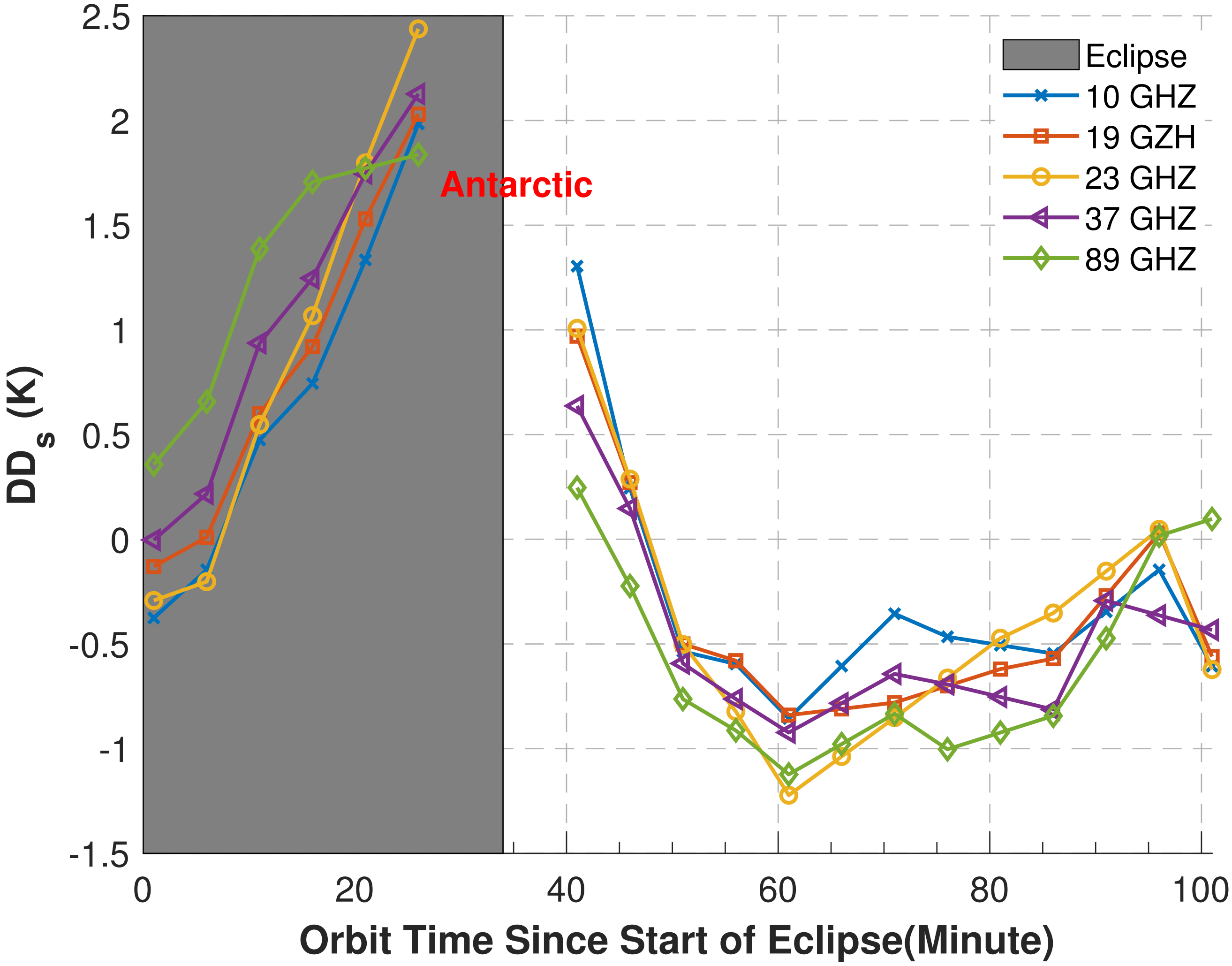

Fig. 4. DD_s as a function of orbit time at MWRI vertical polarization channels with solar beta angle ranging from 20° to 22° for one year (2013).

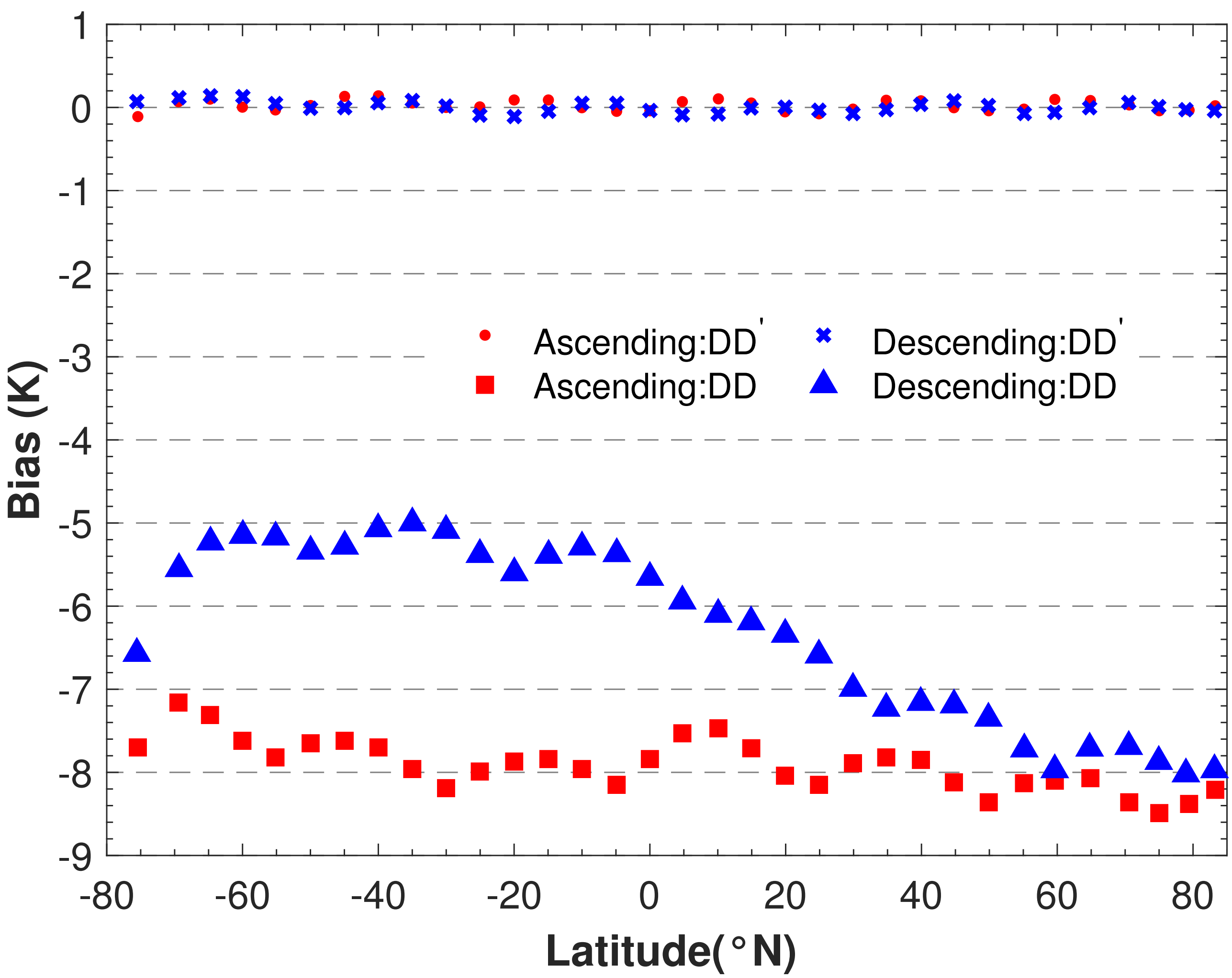

Fig. 5. DD and DD′ at 37V channel between MWRI and AMSR2 as a function of latitude for two years from 2013 to 2014.

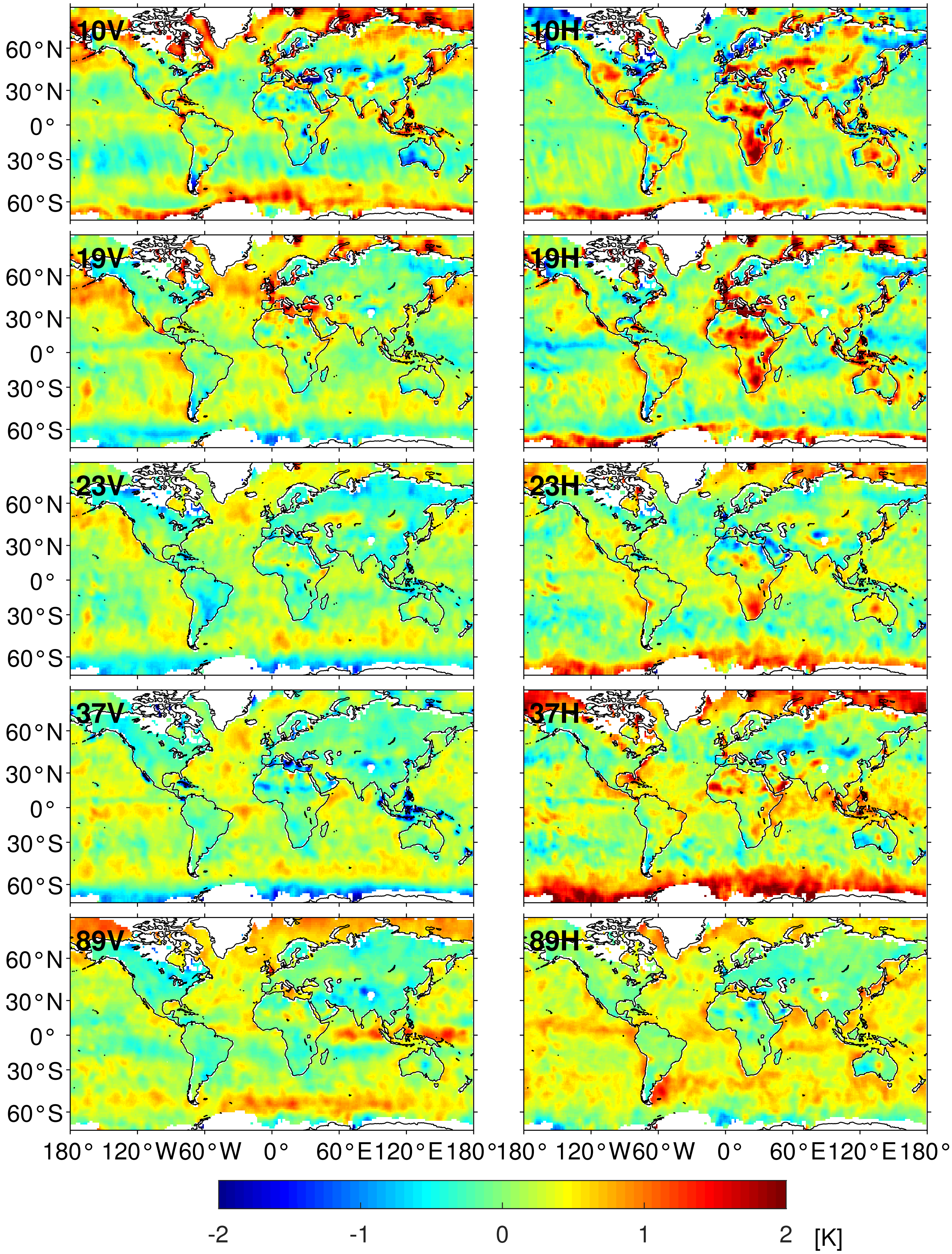

Fig. 6. Global distribution of residual biases between AMSR2 TB and corrected MWRI TB for SCO pairs from July 2012 to December 2012 at vertical (left panel) and horizontal (right panel) polarization channels from 10GHZ (top) to 89GHZ (bottom)

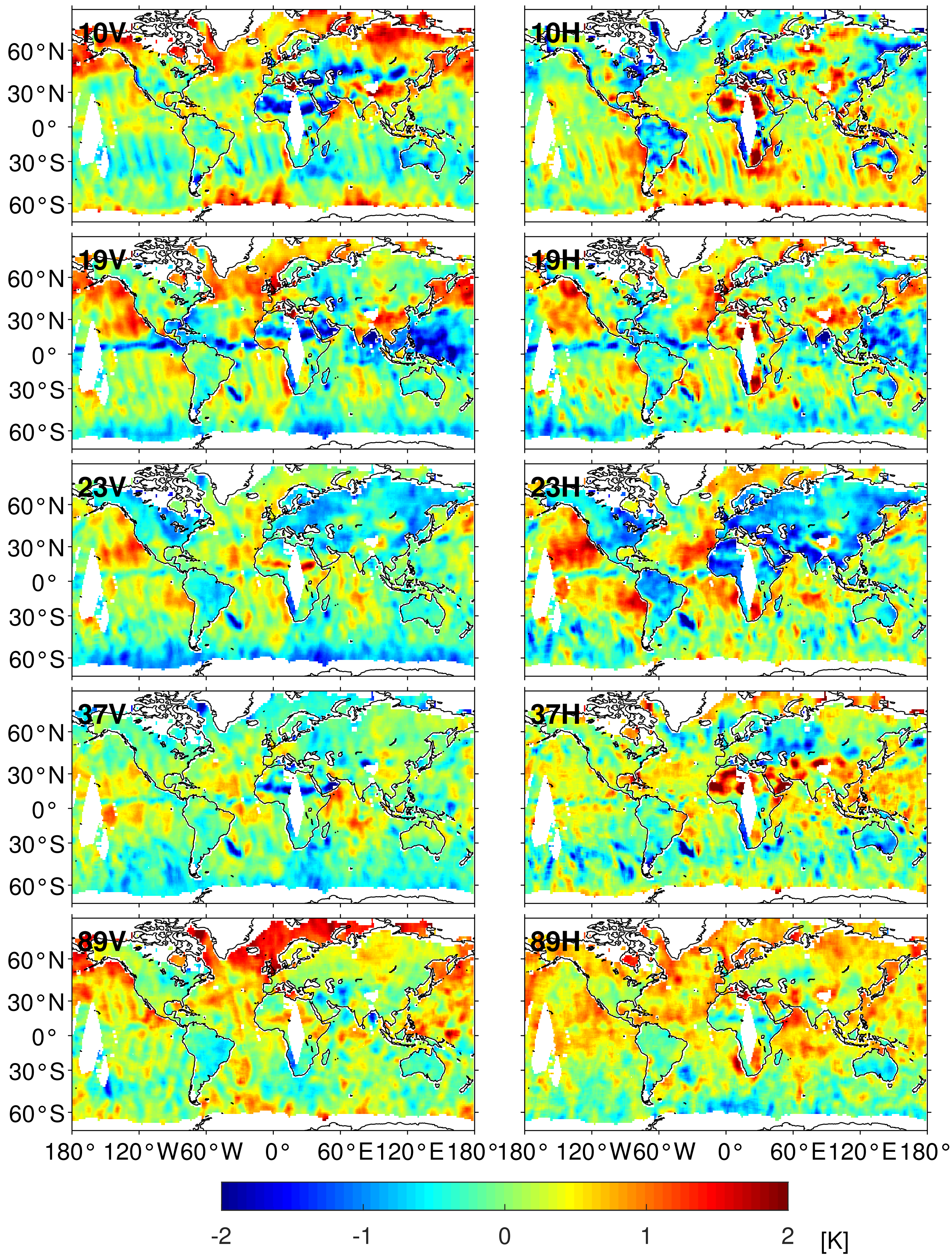

Fig. 7. Global distribution of residual biases between corrected MWRI TB and AMSR-E TB for SCO pairs in June 2011 at vertical (left pannel) and horizontal(right pannel) polarization channels from 10GHZ (top) to 89GHZ (bottom).

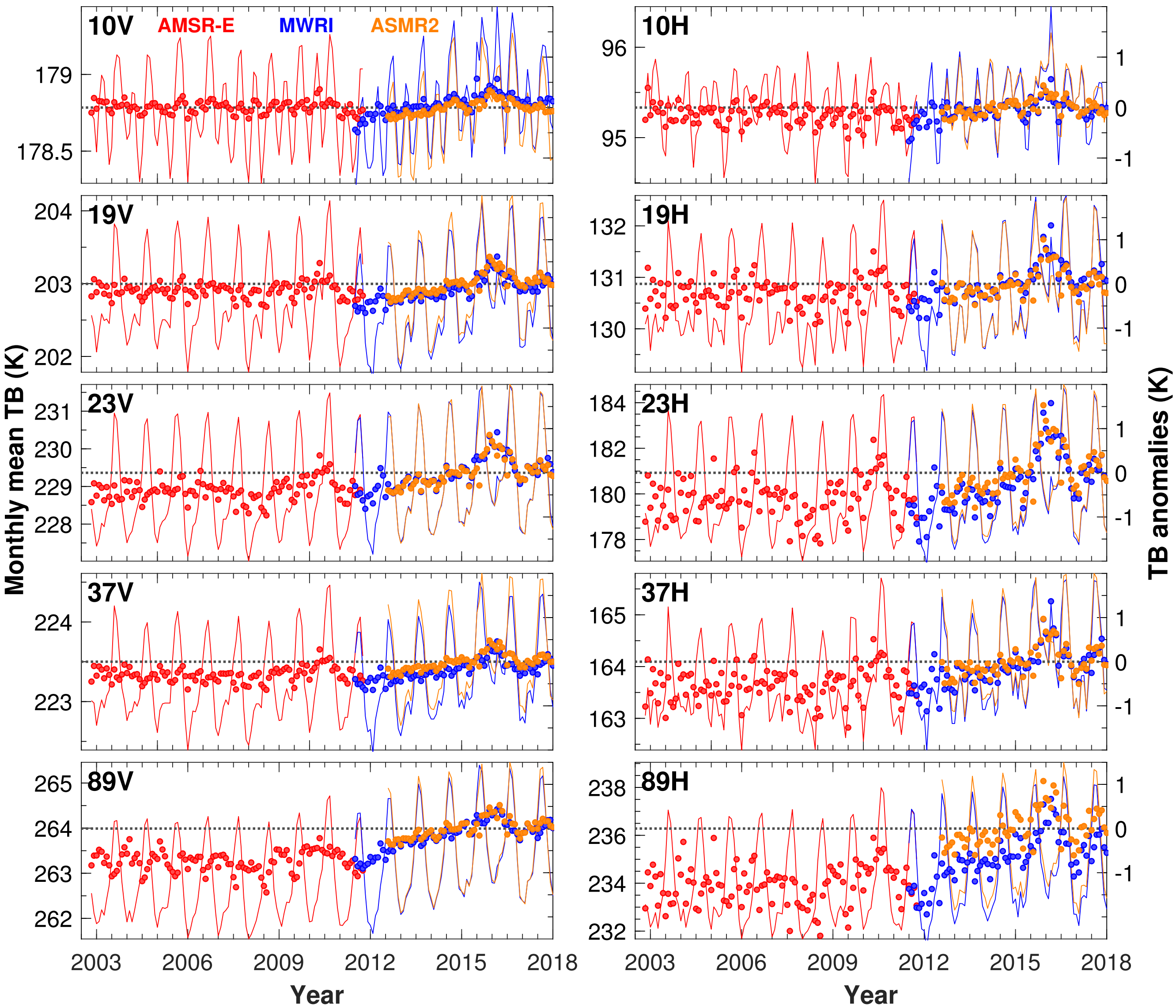

Fig. 8. The monthly mean inter-calibrated TB time series (lines) with their anomalies (dots) for the three sensors over the 60°S-60°N oceanic rain-free areas at vertical (left panel) and horizontal (right panel) polarization channels from 10GHZ (top) to 89GHZ (bottom).

TABLE I
QUALITY FILTERS FOR GRID DATA USED IN DD METHOD

Notes	Ocean	Land
CLW	0-1mm	0-1mm
STD of H-pol channel	0-3K	0-3K
STD of V-pol channel	0-2K	0-2K
WS	0-10m/s	N/A
TB_{19V}-TB_{37V}	N/A	Less than 10K
TB_{19V}	Less than 240K	N/A
TB_V-TB_H	N/A	0-2K

TABLE II
SYSTEMATIC CONSTANT BIASES BETWEEN THE AMSR2 AND MWRI

Channel	C[K]
10V	-14.41
10H	-9.37
19V	-16.78
19H	-8.01
23V	-16.68
23H	-12.39
37V	-17.01
37H	-5.13
89V	-4.39
89H	-10.46

TABLE III
MEAN BIASES AND STANDARD DEVIATION BETWEEN CORRECTED MWRI AND AMSR2 TBS WITHIN THE PERIOD OF JULY 2012 TO DECEMBER 2012 AFTER INTER-CALIBRATION OVER OCEAN AND LAND, RESPECTIVELY

Channel	Ocean		Land	
	Mean[K]	STD[K]	Mean[K]	STD[K]
10V	0.36	0.95	0.00	0.92
10H	0.22	1.01	0.16	1.40
19V	0.23	0.60	0.04	0.62
19H	0.18	1.02	0.23	0.94
23V	0.13	0.35	-0.14	0.47
23H	0.22	0.60	0.10	0.63
37V	0.11	0.50	-0.08	0.41
37H	0.36	0.74	0.18	0.72
89V	0.36	0.41	-0.12	0.37
89H	0.38	0.35	0.01	0.36

TABLE IV
REGRESSION COEFFICIENTS FOR DETERMINING BIASES BETWEEN AMSR-E AND CORRECTED MWRI TBS

Channel	b_1	b_0
10V	0.0161	-5.76
10H	0.0044	-2.62
19V	0.0369	-11.37
19H	0.0024	-1.69
23V	0.0479	-14.20
23H	0.0314	-9.74
37V	0.0248	-6.75
37H	0.0174	-5.20
89V	0.0225	-5.95
89H	0.0085	-1.70

TABLE V
MEAN BIASES AND STANDARD DEVIATION BETWEEN CORRECTED MWRI AND CORRECTED AMSR-E TBS IN JUNE 2011 AFTER INTER-CALIBRATION OVER OCEANS AND LANDS, RESPECTIVELY

Channel	Ocean		Land	
	Mean[K]	STD[K]	Mean[K]	STD[K]
10V	0.17	0.65	-0.02	1.16
10H	0.25	0.69	-0.11	1.55
19V	0.00	0.78	-0.05	0.82
19H	0.03	0.85	0.08	1.00
23V	0.00	0.59	-0.38	0.61
23H	0.25	0.76	-0.69	0.77
37V	-0.03	0.60	-0.08	0.59
37H	0.16	0.83	0.13	0.95
89V	0.33	0.66	0.07	0.57
89H	0.36	0.68	0.26	0.63